Sustainable Energy & Fuels

Structural reduced graphene oxide supercapacitors mechanically enhanced with tannic acid

Journal:	*Sustainable Energy & Fuels*
Manuscript ID	SE-ART-12-2019-001299.R1
Article Type:	Paper
Date Submitted by the Author:	05-Dec-2019
Complete List of Authors:	Flouda, Paraskevi; Texas A and M University College Station Yun, Junyeong; Texas A and M University College Station Loufakis, Dimitrios; Texas A and M University College Station Shah, Smit; Texas A and M University System, Chemical Engineering Green, Micah; Texas A&M University College Station, Chemical Engineering Lagoudas, Dimitris C.; Texas A and M University College Station Lutkenhaus, Jodie; Texas A and M University College Station

SCHOLARONE™
Manuscripts

COMMUNICATION

Structural reduced graphene oxide supercapacitors mechanically enhanced with tannic acid

Received 00th January 20xx,
Accepted 00th January 20xx

DOI: 10.1039/x0xx00000x

Paraskevi Flouda,[a] Junyeong Yun,[b] Dimitrios Loufakis,[a] Smit A. Shah,[b] Micah J. Green,[b] Dimitris C. Lagoudas,[a,c] and Jodie L. Lutkenhaus [b,*]

Electrodes that combine energy storage with mechanical performance are desirable for structural and flexible applications. However, conventional electrodes fail to address mechanical performance. Here, noncovalent bonding of graphene/aramid nanofiber electrodes with tannic acid yields a significant improvement in tensile strength and Young's modulus while maintaining good energy storage.

Introduction

Materials with high electrical conductivity and superior mechanical properties are in great demand for flexible, wearable, and structural batteries and supercapacitors.[1, 2] More specifically, structural energy storage devices require electrodes with high electrical conductivity, tensile strength, and Young's modulus to accommodate mechanical stresses.[3, 4] To date, many efforts dedicated to designing conductive electrode materials have been based on carbon nanomaterials, conductive polymers, and metal oxides.[5-7] However, conventional electrode materials have poor load-bearing function and mechanical reliability.

Graphene has been extensively studied as an electrode material for flexible and structural devices due to its high conductivity, capacitance, surface area, and mechanical properties.[8-13] Flexible supercapacitor electrodes based on reduced graphene oxide (rGO)/MnO_2 exhibited an electrical conductivity of 55 S/cm, a specific capacitance of 130 F/g, and stable capacitance values under cyclic bending.[14] As for structural electrodes, reduced graphene oxide (rGO)/carbon nanotube (CNT) wire-shaped supercapacitor electrodes exhibited a conductivity of 211 S/cm, a specific capacitance of ~35 F/g, a tensile strength of 386 MPa, and a Young's modulus of ~5 GPa.[15] Furthermore, our group recently reported functionalized rGO/aramid nanofiber (ANF) structural supercapacitor electrodes. ANFs are derived from bulk Kevlar fibers and are used as building blocks to improve the mechanical performance of composites. The superior mechanical performance of the ANFs results from hydrogen bonding and π-π interactions between the poly(p-phenylene terephthalamide) (PPTA) aligned chains.[16-20] The composites exhibited an electrical conductivity of 3–28 S/cm, specific capacitance of 80-220 F/g, tensile strength of 35-142 MPa and Young's moduli up to 15 GPa.[21-27] Despite the high electrical and electrochemical performance of the rGO-based electrodes, there remains a challenge to improve the mechanical performance without compromising the capacitance.

Mechanical properties may be improved by enhancing the interfacial interactions between the graphene oxide (GO) flakes, and between the GO flakes and the matrix. Non-covalent interactions have been extensively studied as means to improve the mechanical performance of GO-based composites.[8, 28, 29] More specifically, extensive hydrogen bonding through the addition of PVA (polyvinyl(alcohol)) in GO films led to increased tensile strength, Young's modulus, and ultimate strain by 296 %, 178 %, and 100 %, respectively; the hydrogen bonding interactions facilitated load transfer and allowed GO flakes to slide.[30] Elsewhere, coordination bonding induced by the addition of Al^{3+} ions in GO films led to an increased tensile strength by 136 % and increased Young's modulus by 340 %, whereas the ultimate strain decreased by 60 %.[31] The metal ions coordinate with the carboxylic acid groups at the edges of rGO and the carbonyl and hydroxyl groups of rGO, leading to enhanced tensile strength and Young's modulus.[32] However, the combined effects of hydrogen bonding and metal ion coordination bonding on mechanical and energy storage properties are not well understood.

Hydrogen bonding interactions may be improved by functionalizing GO with tannic acid (TA), a highly adhesive molecule. TA is a polyphenol with catechol and pyrogallol units that is extracted from natural plants such as wood, tea leaves, and berries.[33, 34] TA-functionalized GO (GO-TA) improved the mechanical and electrical properties of PVA-based humidity sensors.[35] Addition of 1 wt% GO-TA in PVA led to a 31 % increase in tensile strength, a 34 % increase in Young's modulus, and 57

[a] *Department of Materials Science and Engineering, Texas A&M University, College Station, TX 77843, USA.*
[b] *Artie McFerrin Department of Chemical Engineering Texas A&M University, College Station, TX 77843, USA.*
[c] *Department of Aerospace Engineering, Texas A&M University, College Station, TX 77843, USA.*

† Electronic Supplementary Information (ESI) available: Experimental details, supplementary figures, and videos. See DOI: 10.1039/x0xx00000x

% in ultimate strain.[35] Coordination bonding through the addition of Fe^{3+} ions to GO-TA films led to a remarkable increase in tensile strength and Young's modulus up to 150 % and 520 %, respectively.[33] However, ultimate strain decreased by 70 %.[33] TA alone has been examined as a redox-active molecule for supercapacitors and batteries.[34, 36, 37] rGO/carbonized paper/TA supercapacitor electrodes exhibited a specific capacitance of 186 F/g, with a capacitance retention of 83% after 500 bending cycles.[36] However, none of these cases quantified *both* the mechanical and energy storage properties for TA-containing electrodes.

Here, we investigate the effect of hydrogen and coordination bonding on the mechanical, electrical, and electrochemical properties of rGO/ANF-based electrodes. GO was functionalized with TA and mixed with branched aramid nanofibers (BANFs) to improve the mechanical properties. The nanocomposites were further modified with divalent (Ca^{2+}) and trivalent (Fe^{3+}) ions. The resulting composites exhibited a maximum Young's modulus of 25 GPa and a tensile strength of 140 MPa, which are five-fold and four-fold improvements compared to pure rGO paper, respectively. The electrochemical performance of the composites in a symmetric supercapacitor configuration was investigated. To demonstrate the electrochemical stability under mechanical loads a flexible device was fabricated. This work demonstrates that synergistic interfacial interactions lead to large improvements in mechanical properties while maintaining superior electrical and electrochemical properties.

Results and discussion

Graphene oxide was functionalized with tannic acid by the reaction of GO's epoxide groups with TA's galloyl and catechol groups. GO-TA of different TA contents (1, 3, 5, and 7 wt%) were synthesized. Thermal gravimetric analysis (TGA) is provided in Fig. S1, ESI†. GO-TA dispersions were mixed with branched aramid nanofiber dispersions in dimethyl sulfoxide and free-standing films were fabricated using vacuum filtration. The premade films were modified with metal chloride solutions of Ca^{2+} and Fe^{3+}. The nanocomposites were thermally reduced[38] to yield reduced GO-TA/BANF (rGO-TA/BANF) electrodes.

Digital images of the composites are shown in Fig. 1a. The composites exhibited qualitatively good mechanical performance (Video S1, Video S2, and Video S3, ESI†). Scanning electron microscopy (SEM) images (Fig. 1b and 1c) revealed a highly layered structure with thicknesses of 5-10 µm. rGO-TA flakes interact with BANFs through extensive hydrogen bonding interactions while the Ca^{2+} and Fe^{3+} ions interact with the rGO oxygen groups and the TA galloyl and catechol groups though coordination bonding, as shown in Fig. 1d.The electrodes made from GO with a TA content of 5 wt% were selected for further study since it led to the optimum mechanical performance for rGO-TA papers (without BANFs) (Fig. S2, ESI†). From this point on "GO-TA" implies to a content of 5 wt% TA.

X-ray photoelectron spectroscopy (XPS), energy dispersive X-ray spectroscopy (EDS), Raman spectroscopy, and X-ray diffraction (XRD) were utilized to verify the chemical modifications and interactions. Fig. 2a shows the XPS survey scans for rGO/10 wt% BANF, rGO-TA/10 wt% BANF, rGO-TA/10 wt% BANF/Ca^{2+}, and rGO-TA/10 wt% BANF/Fe^{3+}. TA functionalization caused a decrease in the C/O ratio from 4.6 to 3.1 (rGO/10 wt% BANF *vs.* rGO-TA/10 wt% BANF) resulting from the TA oxygen moieties.[35] Addition of Ca^{2+} and Fe^{3+} ions led to a slightly decreased C/O ratio of 2.9 and 2.7, respectively, due to the acidic nature of the metal chlorides (Table S1, ESI†).[32, 33] Moreover, Ca^{2+} and Fe^{3+} peaks appeared in the survey scans, indicating the successful addition of the metal ions corresponding to 1.5 at % and 2.9 at %, respectively (Fig. 2a and Fig. S3, ESI†). Fe^{3+} addition was verified also using SEM-EDS mapping, as shown in Fig. 2c, 2d and Fig. S4, ESI†.

The characteristic D (1347 cm^{-1}) and G (1602 cm^{-1}) bands for carbon-based materials were apparent in the Raman spectra, Fig 2b.[39, 40] The D band is attributed to defects such as sp^3-hybridized carbon atoms, whereas the G band derives from the sp^2-hybridized carbon atoms. The D/G intensity ratio is used to qualitatively characterize defects.[40] TA functionalization led to an increase in I_D/I_G from 0.93 to 0.95 resulting from the partial reduction of the GO flakes.[41] Ca^{2+} and Fe^{3+} modifications did not cause significant changes in the I_D/I_G values.

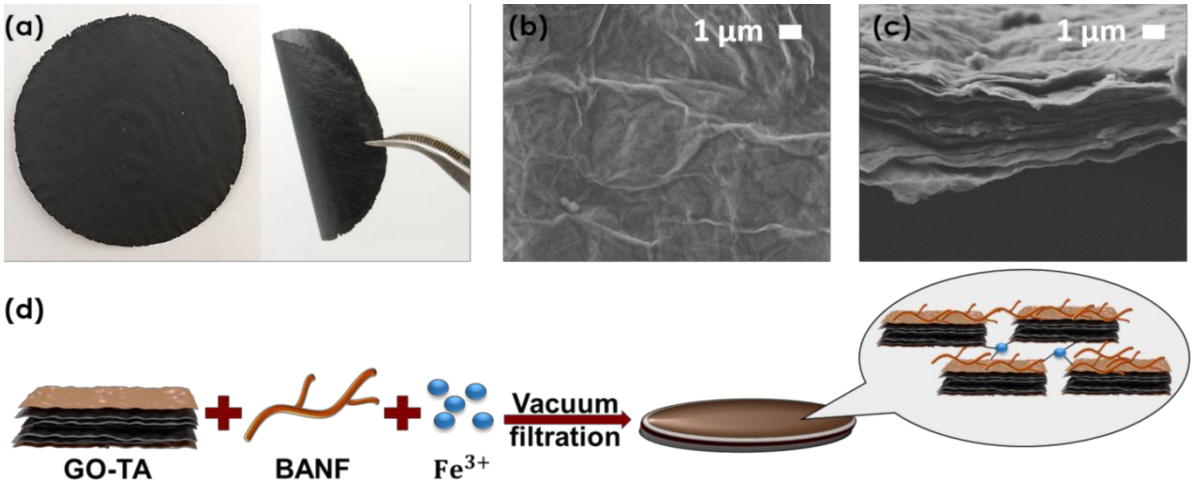

Fig. 1 (a) Digital images of the composite electrodes. Scanning electron microscopy images of the (b) top and (c) cross-section of rGO-TA/10 wt% BANF. (d) Schematic representation of the rGO-TA/BANF composites.

This journal is © The Royal Society of Chemistry 20xx

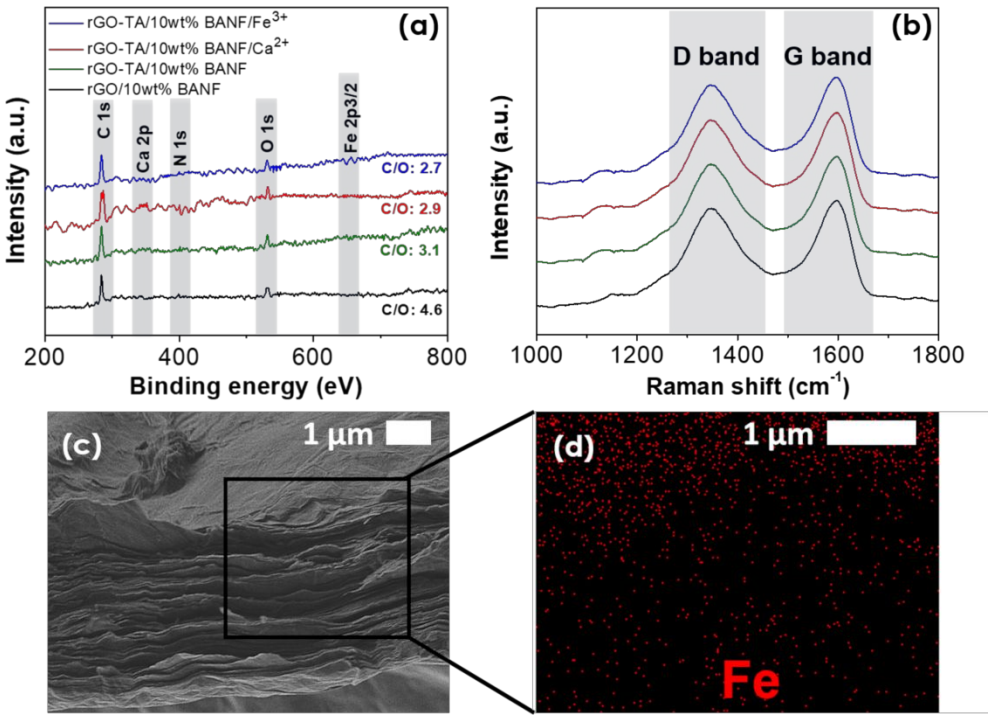

Fig. 2 (a) XPS survey scans and (b) Raman spectra for rGO/10 wt% BANF, rGO-TA/10 wt% BANF, rGO-TA/10 wt% BANF/Ca^{2+}, and rGO-TA/10 wt% BANF/Fe^{3+}. The legend in (a) applies also for (b). (c) Cross-sectional SEM image and (d) EDS mapping of Fe element for rGO-TA/10 wt% BANF/Fe^{3+}.

High-resolution XPS N1s and C1s peaks were used to verify the interfacial interactions between rGO-TA and BANFs. TA functionalization led to an increase in the hydrogen bonding peak of the N1s spectra at 401.8 eV (Fig. S5, ESI†).[26] More specifically, rGO-TA and BANFs interact with each other through extensive hydrogen bonding interactions between the rGO oxygen groups, the TA galloyl and catechol groups, and the BANF amide groups. Metal ions interact with the rGO oxygen groups and the TA galloyl and catechol groups though coordination bonding.[33] These interactions were verified from the shift of the -COOH peak of the C1s peak after the addition of the Ca^{2+} and Fe^{3+} ions from 288.7 eV to 289.0 eV and 289.2 eV, respectively (Fig. S6, ESI†).

To further elucidate the interactions, XRD was performed, Fig. S7 and Table S2, ESI†. The d-spacing decreased from 0.439 nm to 0.423 nm with the TA functionalization for the BANF-containing composites, indicating that the TA molecules wrap around the rGO flakes. Ca^{2+} and Fe^{3+} modified composites exhibited also a decreased d-spacing of 0.417 nm and 0.413 nm, respectively, resulting from the strong interactions between the rGO-TA flakes.[42, 43]

Typical stress-strain curves of the composite films are shown in Fig. 3a. Those curves were used to calculate the ultimate tensile strength, Young's modulus, toughness, and ultimate strain, as shown in Fig. 3b, 3c, Fig. S8, and Table S3, ESI†. TA functionalization led to an 80 % increase (from 5 GPa to 9 GPa) in Young's modulus and 123 % increase (from 35 to 78 MPa) in ultimate tensile strength compared to rGO. Ultimate strain and toughness increased by 25 % (from 0.8 to 1.0 %) and 250 % (from 120 to 420 kJ/m^3), respectively. Such increases result from the enhanced hydrogen bonding interactions between the galloyl and catechol groups of the TA functionalized rGO flakes.[33, 35] Addition of BANFs up to 10 wt% led to a further increase in Young's modulus of ~90 % (17 GPa) and an 80 % (140 MPa) increase in ultimate tensile strength, due to the stiff and load-bearing BANFs.[22] Toughness and ultimate strain exhibited a similar trend. Further increase in the BANF composition (to 15 wt% and 25 wt%) did not lead to improvements in the mechanical properties due to possible aggregation of the BANFs.

Additionally, the rGO-TA/10 wt% BANF composites were modified with divalent (Ca^{2+}) and trivalent ions (Fe^{3+}). Young's modulus increased further by ~12 % (19 GPa, within error) and ~70 % (25 GPa) when Ca^{2+} and Fe^{3+} ions were added, respectively. No changes were observed in the ultimate tensile strength, and the toughness retained its high values whereas the ultimate strain decreased up to 10 % for Ca^{2+} and 37 % for Fe^{3+}. The TA hydroxyl groups provide binding sites for the metal ions to bind and coordinate leading to extensive cross-linking between the functionalized rGO flakes.[33] These modifications prevent the rGO flakes from sliding leading to lower ultimate strains but significantly higher Young's moduli.[33, 44] The Fe^{3+}-containing composites exhibited superior mechanical performance compared to the Ca^{2+}-containing composites resulting from the higher valency that leads to stronger attraction.[45] Therefore, we focus on the Fe^{3+} containing composites.

To further elucidate the mechanism for the improved mechanical performance, additional tensile testing on rGO/Fe^{3+} (without BANFs) and rGO/10 wt% BANF/Fe^{3+} was conducted, as shown in Table S3 and Fig. S9, ESI†. The rGO/Fe^{3+} electrodes exhibited a Young's modulus of 6.5 GPa and tensile strength of 40 MPa, which corresponds to a 30 % and 14 % increase compared to the pure rGO films (without BANFs).[23] However, these properties are lower than the rGO-TA composites due to the absences of the extensive hydrogen bonding afforded by the TA. rGO/10 wt% BANF/Fe^{3+} films exhibited a Young's modulus and tensile strength of 12 GPa and 97 MPa, which is 70

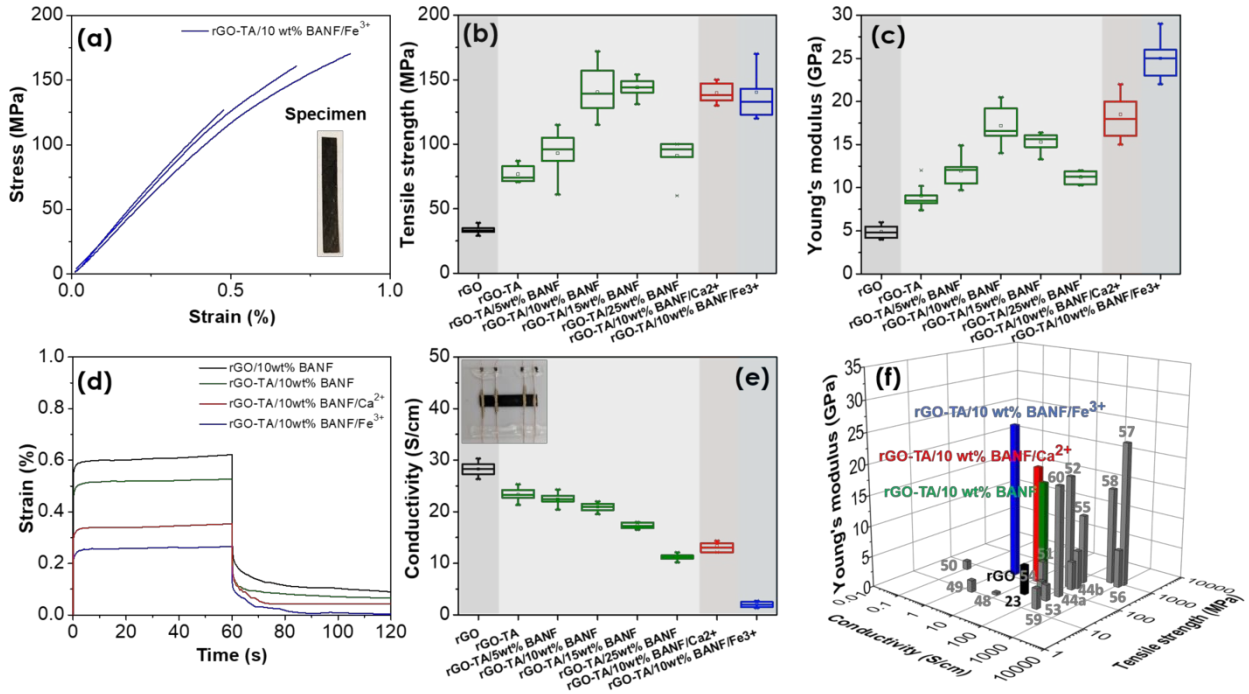

Fig. 3 (a) Typical stress-strain curves for rGO-TA/10 wt% BANF/Fe^{3+}. Inset shows a specimen used for tensile testing. Box plots of (b) tensile strength and (c) Young's modulus. (d) Creep recovery testing for rGO/10 wt% BANF, rGO-TA/10 wt% BANF, rGO-TA/10 wt% BANF/Ca^{2+}, and rGO-TA/10 wt% BANF/Fe^{3+} electrodes at 40 MPa. (e) Box plots of electrical conductivity. Inset shows the sample preparation for the conductivity measurements. (f) Ashby plot of Young's modulus *vs.* electrical conductivity *vs.* tensile strength for mechanically strong conductive materials. Grey points represent data obtained from the literature and the numbers correspond to references in the main text. See Fig. S10, ESI† for 2-D representations of the Ashby plot.

% and 21 % more than the rGO/10 wt% BANF, and 52 % and 31 % less than the TA modified films (rGO-TA/10 wt% BANF/Fe^{3+}).[26] The results reveal the synergistic effect of the enhanced hydrogen and coordination bonding due to the TA functionalization and multivalent ion modification that leads to enhanced mechanical properties.

Furthermore, creep recovery testing was conducted for rGO/10 wt% BANF, rGO-TA/10 wt% BANF, rGO-TA/10 wt% BANF/Ca^{2+}, and rGO-TA/10 wt% BANF/Fe^{3+} electrodes, Fig. 3d. Creep recovery tests are used to study the relative slipping of the rGO flakes within the composite.[30] The unmodified composites (rGO/10 wt% BANF) exhibited the highest creep and residual recovery strains, followed by rGO-TA/10 wt% BANF and the metal ion modified composites. The results indicate that the TA and Fe^{3+} modifications led to stronger adhesion between the rGO flakes that restrained their slippage.[46]

The electrical conductivity of the rGO and rGO-TA composites was measured using a 4-point sensing method, as shown in Fig 3e. TA functionalization led to an 18 % decrease in conductivity (from 28 S/cm to 23 S/cm) due to the addition of a non-conductive molecule (TA).[47] The conductivity further decreased by 9 % (21 S/cm) as a result of the addition of 10 wt% BANFs, since BANFs are not electrically conductive and disrupt the conductive rGO pathways.[27] Further addition of BANF (15-25 wt%) led to a significant drop in conductivity (11 S/cm). The metal ion modifications also led to deteriorated electrical conductivity resulting from the metal chloride treatment and the disruption of the conductive pathways.[47]

Fig. 3f, Fig. S10, and Table S4, ESI† illustrate an Ashby plot of the Young's modulus *vs.* electrical conductivity *vs.* tensile strength for mechanically strong conductive nanocomposites. The rGO-TA composites exhibited a good combination of mechanical and electrical properties as shown also in Video S4, ESI†. Trade-offs due to TA functionalization and metal ion modification are apparent. More specifically, these modifications (<10 wt% BANF) led to an increased Young's modulus, tensile strength but deteriorated electrical conductivity. The properties of the TA composites were compared against other state-of-the-art conductive nanocomposites.[48-51] More specifically, rGO-polyacrylic acid (PAA),[52] rGO-polydopamine (PDA),[44] rGO-PDA/Ni^{2+},[44] polypyrrole (PPy)/rGO,[53] rGO/MnO_2/carbon nanotube (CNTs),[54] rGO-10,12-pentacosadiyn-1-ol (PCO)/Zn^{2+},[55] rGO-cellulose nanocrystal (CNC),[56] pBG,[57] SBG,[58] mutli-walled CNTs (MWCNTs),[59] and single-walled CNTs (SWCNTs)-PPy-cyanate ester (CE)[60] exhibited higher conductivity values. However, the TA composites maintained high conductivities, tensile strength, and exhibited significantly higher Young's moduli as a result of the strong interactions with the stiff BANFs and coordination bonding.

The electrochemical performance of selected composite films as supercapacitor electrodes was investigated. More specifically, the composites with the highest electrical conductivity (rGO), highest Young's modulus and tensile strength (rGO-TA/10 wt% BANF/Fe^{3+}), and best combination of these properties (rGO-TA/10 wt% BANF) were examined. Two-electrode symmetric coin cells with 6M KOH as the electrolyte were assembled (Fig. 4a). The electrode stability in the electrolyte was verified using UV-Vis spectroscopy, as shown in Fig. S11, ESI†. Fig. 4b shows the cyclic voltammograms for rGO-TA/10 wt% BANF/Fe^{3+} at different scan rates (1-100 mV/s). rGO exhibited the highest specific capacitance (216 ± 11 F/g) at 1 mV/s.[23] TA functionalization and BANF addition (10 wt%) led to a deteriorated specific capacitance of 120 ± 8 F/g, resulting from

This journal is © The Royal Society of Chemistry 20xx

Please do not adjust margins

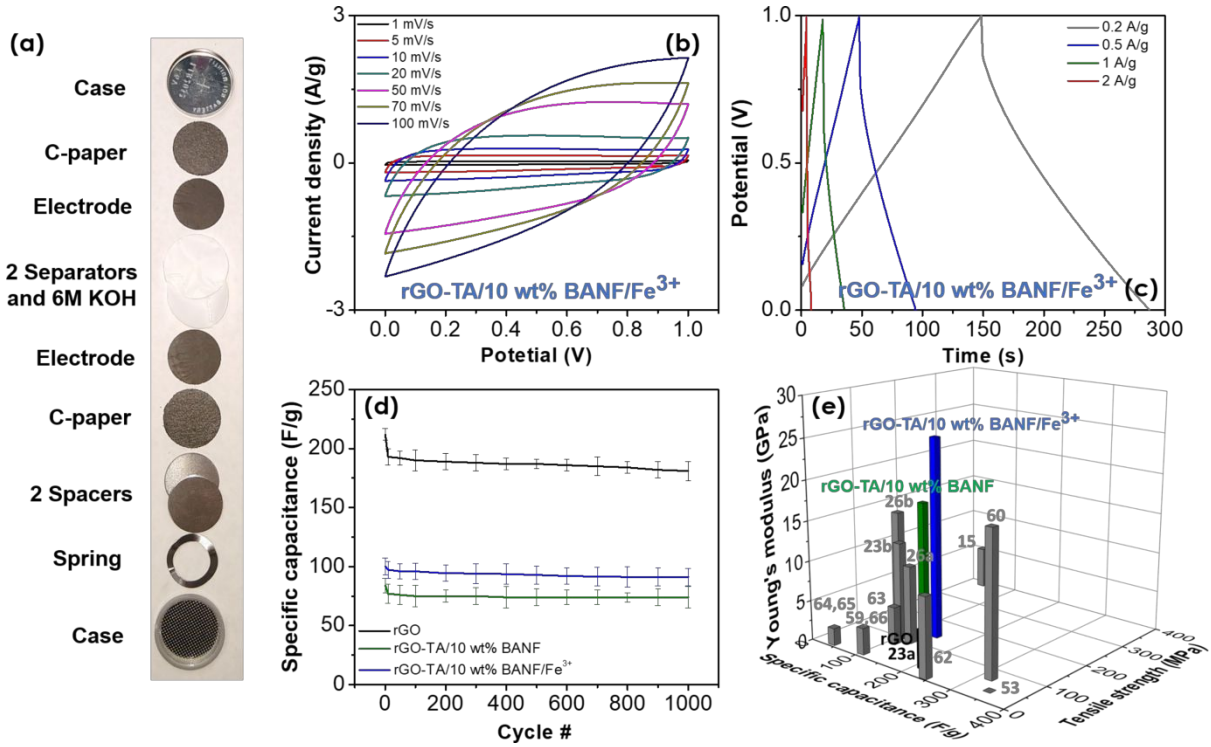

Fig. 4 (a) Digital image of the parts of a 2-electrode symmetric coin cell. (b) Cyclic voltammetry curves at different scan rates (1-100 mV/s) and (c) galvanostatic charge-discharge curves at different current densities (0.2-2 A/g) for rGO-TA/10 wt% BANF/Fe^{3+}. (d) Specific capacitance *vs.* cycle number at 0.5 A/g for 1000 cycles. (e) Ashby plot of Young's modulus *vs.* specific capacitance *vs.* tensile strength for mechanically strong supercapacitor electrodes.

the decreased electrical conductivity and diffusion limitations due to the more compact structure.[61] Addition of Fe^{3+} ions led to improved specific capacitance (145 ± 9 F/g) despite the low electrical conductivity of the composites. The improvement is attributed to the better wettability of the Fe^{3+} ion modified electrodes, as observed from the contact angle experiments (Fig. S12 and Table S5, ESI†). Increasing the scan rate led to a decrease in specific capacitance due to diffusion limitations for all electrodes investigated, as shown in Table S6, ESI†.[61]

Galvanostatic charge-discharge tests at variant current densities (0.2-2 A/g) were also conducted, as shown in Fig. 4c. The curves exhibited triangular shapes and the discharge time decreased with current density. Prolonged charge-discharge tests at 0.5 A/g for 1000 cycles were conducted (Fig. 4d and Table S7, ESI†). The electrodes exhibited good electrochemical stability with a capacitance retention of 85 % for rGO, 89 % for rGO-TA/10 wt% BANF, and 91 % rGO-TA/10 wt% BANF/Fe^{3+}. Ragone plots (specific energy *vs.* specific power and energy density *vs.* power density) were constructed, Fig. S13, ESI†. Pure rGO (no BANFs) exhibited the highest specific energy and energy density, while rGO-TA/10 wt% BANF and rGO-TA/10 wt% BANF/Fe^{3+} exhibited lower values.

Fig. 4e, Fig. S14, and Table S8, ESI† illustrate Ashby plots of the Young's modulus *vs.* specific capacitance *vs.* tensile strength for mechanically strong supercapacitor electrodes.[15, 23, 53, 59, 60, 62-66] The TA composites exhibited a better combination of properties compared against other rGO containing composites such as rGO/CNT,[15] rGO-NH_2/ANF,[23] and rGO-dopamine (DOPA)[26] because of the stronger synergistic interfacial interactions. rGO,[23] rGO/MnO_2[62] and SWCNT-PPy-CE[60] exhibited higher specific capacitance than the rGO-TA/10 wt% BANF composites. However, the rGO-TA/10 wt% BANF/Fe^{3+} electrodes maintained high specific capacitance and tensile strength values with a superior Young's modulus. To demonstrate the combination of mechanical and electrochemical properties the multifunctional efficiency was calculated, as shown in Table S9, ESI†. The rGO-TA-based composite films exhibited a multifunctional efficiency significantly higher than 1 when compared against epoxy and carbon aerogel indicating mass and volume savings.[67, 68]

At this point, it is worth mentioning research efforts elsewhere focused upon activated carbon fibers as structural supercapacitor electrodes. The carbon fiber-based electrodes exhibit significantly higher mechanical properties (tensile strength of 3960 MPa and Young's modulus of 207 GPa), but they suffer from low electrochemically active surface area leading to extremely poor electrochemical performance (*e.g.,* specific capacitance of 2.63 F/g).[69] Additionally, other researchers have focused on different device architectures such as spine-like or accordion-like batteries to combine good mechanical performance with energy storage.[70, 71]

A prototype flexible device was fabricated to display the energy storage capability of the electrodes while bearing mechanical loads. The rGO-TA/10 wt% BANF/Fe^{3+} composites were used as the electrodes, and H_3PO_4-polyvinyl(alcohol) (PVA) gel was the electrolyte (Fig. 5a). Electrochemical testing was conducted in flat and in bent states (bending radius: 0.6 cm) using cyclic voltammetry at a scan rate of 20 mV/s, as shown in Fig. 5b. The cyclic voltammograms exhibited a distorted profile resulting from limited ion diffusion rates typical for gel electrolytes.[72, 73] Cyclic bending up to 100 cycles had no significant effect on the CV curves and the initial specific capacitance (48 F/g), as shown in Fig. 5c and Table S10, ESI†. The results indicate excellent electrochemical stability when mechanical loads are applied. Cyclic voltammetry at lower scan

rates showed significantly higher specific capacitances- up to 120 F/g at 1 mV/s, as shown in Fig. 5d, 5e, and 5f.

Conclusions

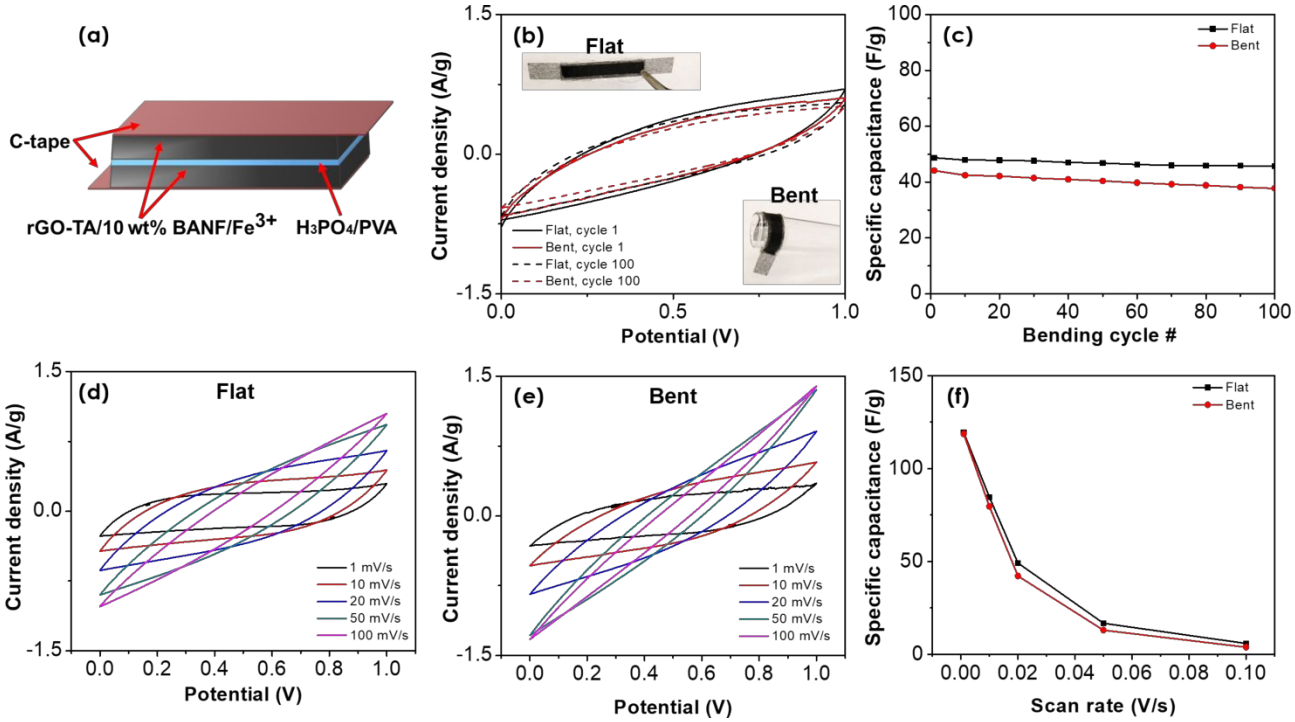

Fig. 5 (a) Schematic representation of the flexible device. (b) Cyclic voltammetry curves for the rGO-TA/10 wt% BANF/Fe^{3+} flexible supercapacitor at 20 mV/s in flat and bent states. (c) Specific capacitance *vs.* bending cycle. Cyclic voltammetry curves at variant scan rates (1 - 100 mV/s) in (d) flat and (e) bent states. (f) Specific capacitance *vs.* scan rate for the rGO-TA/10 wt% BANF/Fe^{3+} flexible device in flat and bent states.

Electrodes with superior mechanical performance were fabricated by simultaneously leveraging hydrogen bonding and metal ion coordination bonding interactions. rGO/BANF electrodes were modified with tannic acid to enhance the hydrogen bonding interactions and multivalent ions were introduced to create coordination bonding. More specifically, the metal ions coordinate with the carboxylic acid groups at the edges of rGO. Additionally, they interact through alkoxide bonds with the carbonyl and hydroxyl groups of rGO and the tannic acid galloyl and catechol groups. The modified electrodes exhibited a five-fold increase in Young's modulus and a four-fold increase in tensile strength compared to pure rGO (no BANFs) as a result of the synergy of the different interfacial interactions that lead to stronger adhesion between the rGO flakes. Moreover, the electrodes maintained high electrical conductivity and capacitance making them ideal candidates for structural or even flexible electrodes. These results demonstrate that synergistic bonding leads to tremendous enhancements in mechanical performance while maintaining the energy storage ability of the next-generation electrodes.

Conflicts of interest

There are no conflicts to declare.

Acknowledgements

The authors acknowledge the TAMU Materials Characterization Facility. J.L.L. acknowledges the William and Ruth Neely Faculty Fellowship. This work was supported by Air Force Office of Scientific Research Grant No. FA9550-19-1-0170. The authors thank Prof. James G. Boyd of Texas A&M University and Prof. Haleh Ardebili of University of Houston for their helpful discussions.

References

1. X. Peng, L. Peng, C. Wu and Y. Xie, *Chemical Society Reviews*, 2014, **43**, 3303-3323.
2. W. Liu, M.-S. Song, B. Kong and Y. Cui, *Advanced Materials*, 2017, **29**, 1603436.
3. L. E. Asp and E. S. Greenhalgh, *Composites Science and Technology*, 2014, **101**, 41-61.
4. L. E. Asp, *Plastics Rubber and Composites*, 2013, **42**, 144-149.
5. X. Lu, M. Yu, G. Wang, Y. Tong and Y. Li, *Energy & Environmental Science*, 2014, **7**, 2160-2181.
6. Q. Wu, Y. Xu, Z. Yao, A. Liu and G. Shi, *ACS Nano*, 2010, **4**, 1963-1970.
7. J. Jiang, Y. Li, J. Liu, X. Huang, C. Yuan and X. W. Lou, *Advanced Materials*, 2012, **24**, 5166-5180.
8. D. A. Dikin, S. Stankovich, E. J. Zimney, R. D. Piner, G. H. B. Dommett, G. Evmenenko, S. T. Nguyen and R. S. Ruoff, *Nature*, 2007, **448**, 457.
9. A. K. Geim and K. S. Novoselov, *Nat Mater*, 2007, **6**, 183-191.
10. S. A. Shah, D. Kulhanek, W. Sun, X. Zhao, S. Yu, D. Parviz, J. L. Lutkenhaus and M. J. Green, *Journal of Colloid and Interface Science*, 2019, DOI: https://doi.org/10.1016/j.jcis.2019.10.066.
11. W. Sun, S. A. Shah, J. L. Lowery, J. H. Oh, J. L. Lutkenhaus and M. J. Green, *Advanced Materials Interfaces*, **0**, 1900786.
12. Y. He, P. Zhang, M. Wang, F. Wang, D. Tan, Y. Li, X.

This journal is © The Royal Society of Chemistry 20xx

Please do not adjust margins

Zhuang, F. Zhang and X. Feng, *Materials Horizons*, 2019, **6**, 1041-1049.
13. M. Yang, Z. Xu, P. Li, F. Guo, Y. Liu, Y. Xiao, W. Gao and C. Gao, *Materials Horizons*, 2018, **5**, 1112-1119.
14. Y. He, W. Chen, X. Li, Z. Zhang, J. Fu, C. Zhao and E. Xie, *ACS Nano*, 2013, **7**, 174-182.
15. Y. Ma, P. Li, J. W. Sedloff, X. Zhang, H. Zhang and J. Liu, *ACS Nano*, 2015, **9**, 1352-1359.
16. M. Yang, K. Cao, L. Sui, Y. Qi, J. Zhu, A. Waas, E. M. Arruda, J. Kieffer, M. D. Thouless and N. A. Kotov, *ACS Nano*, 2011, **5**, 6945-6954.
17. M. Yang, K. Q. Cao, B. Yeom, M. D. Thouless, A. Waas, E. M. Arruda and N. A. Kotov, *J Compos Mater*, 2015, **49**, 1873-1879.
18. J. Lyu, X. Z. Wang, L. H. Liu, Y. Kim, E. K. Tanyi, H. Chi, W. C. Feng, L. Z. Xu, T. H. Li, M. A. Noginov, C. Uher, M. D. Hammig and N. A. Kotov, *Adv Funct Mater*, 2016, **26**, 8435-8445.
19. J. Zhu, M. Yang, A. Emre, J. H. Bahng, L. Xu, J. Yeom, B. Yeom, Y. Kim, K. Johnson, P. Green and N. A. Kotov, *Angewandte Chemie International Edition*, 2017, **56**, 11744-11748.
20. J. Lyu, M. D. Hammig, L. H. Liu, L. Z. Xu, H. Chi, C. Uher, T. H. Li and N. A. Kotov, *Appl Phys Lett*, 2017, **111**, 161901.
21. S. R. Kwon, M. B. Elinski, J. D. Batteas and J. L. Lutkenhaus, *ACS Appl Mater Interfaces*, 2017, **9**, 17125-17135.
22. S. R. Kwon, J. Harris, T. Zhou, D. Loufakis, J. G. Boyd and J. L. Lutkenhaus, *ACS Nano*, 2017, **11**, 6682-6690.
23. P. Flouda, X. Y. Feng, J. G. Boyd, E. L. Thomas, D. C. Lagoudas and J. L. Lutkenhaus, *Batteries & Supercaps*, 2019, **2**, 464-472.
24. T. Zhou, J. G. Boyd, J. L. Lutkenhaus and D. C. Lagoudas, *Acta Mech*, 2018, **230**, 265-280.
25. A. G. Patel, L. Johnson, R. Arroyave and J. L. Lutkenhaus, *Mol Syst Des Eng*, 2019, **4**, 654-663.
26. P. Flouda, S. A. Shah, D. C. Lagoudas, M. J. Green and J. L. Lutkenhaus, *Matter*, 2019, DOI: https://doi.org/10.1016/j.matt.2019.09.017.
27. Z. Tianyang, G. B. James, L. Dimitrios, L. Jodie and C. L. Dimitris, *Smart Materials and Structures*, 2019.
28. Y. Xu, H. Bai, G. Lu, C. Li and G. Shi, *Journal of the American Chemical Society*, 2008, **130**, 5856-5857.
29. Q. Cheng, L. Jiang and Z. Tang, *Accounts of Chemical Research*, 2014, **47**, 1256-1266.
30. L. Liu, Y. Gao, Q. Liu, J. Kuang, D. Zhou, S. Ju, B. Han and Z. Zhang, *Small*, 2013, **9**, 2466-2472.
31. C.-N. Yeh, K. Raidongia, J. Shao, Q.-H. Yang and J. Huang, *Nature Chemistry*, 2015, **7**, 166.
32. S. Park, K.-S. Lee, G. Bozoklu, W. Cai, S. T. Nguyen and R. S. Ruoff, *ACS Nano*, 2008, **2**, 572-578.
33. R.-Y. Liu and A.-W. Xu, *RSC Advances*, 2014, **4**, 40390-40395.
34. C. Wu, T. Li, C. Liao, L. Li and J. Yang, *Journal of Materials Chemistry A*, 2017, **5**, 12782-12786.
35. M.-Y. Lim, H. Shin, D. M. Shin, S.-S. Lee and J.-C. Lee, *Polymer*, 2016, **84**, 89-98.
36. M.-Y. Jia, L.-S. Xu, Y. Li, C.-L. Yao and X.-J. Jin, *New Journal of Chemistry*, 2018, **42**, 14576-14585.
37. L. Pan, H. Wang, C. Wu, C. Liao and L. Li, *ACS Applied Materials & Interfaces*, 2015, **7**, 16003-16010.
38. D. R. Dreyer, S. Park, C. W. Bielawski and R. S. Ruoff, *Chemical Society Reviews*, 2010, **39**, 228-240.
39. K. N. Kudin, B. Ozbas, H. C. Schniepp, R. K. Prud'homme, I. A. Aksay and R. Car, *Nano Lett*, 2008, **8**, 36-41.
40. A. C. Ferrari and D. M. Basko, *Nature Nanotechnology*, 2013, **8**, 235-246.
41. Y. Lei, Z. Tang, R. Liao and B. Guo, *Green Chemistry*, 2011, **13**, 1655-1658.
42. W. Zheng, R. Tan, L. Zhao, Y. Chen, C. Xiong and D. Yin, *RSC Advances*, 2014, **4**, 11732-11739.
43. L. Chen, G. Shi, J. Shen, B. Peng, B. Zhang, Y. Wang, F. Bian, J. Wang, D. Li, Z. Qian, G. Xu, G. Liu, J. Zeng, L. Zhang, Y. Yang, G. Zhou, M. Wu, W. Jin, J. Li and H. Fang, *Nature*, 2017, **550**, 380.
44. S. Wan, F. Xu, L. Jiang and Q. Cheng, *Advanced Functional Materials*, 2017, **27**, 1605636.
45. T. Benselfelt, M. Nordenström, S. B. Lindström and L. Wågberg, *Advanced Materials Interfaces*, 2019, **6**, 1900333.
46. Y. Gao, L.-Q. Liu, S.-Z. Zu, K. Peng, D. Zhou, B.-H. Han and Z. Zhang, *ACS Nano*, 2011, **5**, 2134-2141.
47. T. Kuila, S. Bose, A. K. Mishra, P. Khanra, N. H. Kim and J. H. Lee, *Progress in Materials Science*, 2012, **57**, 1061-1105.
48. C. Sasso, E. Zeno, M. Petit-Conil, D. Chaussy, M. N. Belgacem, S. Tapin-Lingua and D. Beneventi, *Macromolecular Materials and Engineering*, 2010, **295**, 934-941.
49. F. M. Blighe, D. Diamond, J. N. Coleman and E. Lahiff, *Carbon*, 2012, **50**, 1447-1454.
50. X. Han, L. Lv, D. Yu, X. Wu and C. Li, *ACS Applied Materials & Interfaces*, 2019, **11**, 3466-3473.
51. M. Hou, M. Xu and B. Li, *ACS Sustainable Chemistry & Engineering*, 2018, **6**, 2983-2990.
52. S. Wan, H. Hu, J. Peng, Y. Li, Y. Fan, L. Jiang and Q. Cheng, *Nanoscale*, 2016, **8**, 5649-5656.
53. S. Li, C. Zhao, K. Shu, C. Wang, Z. Guo, G. G. Wallace and H. Liu, *Carbon*, 2014, **79**, 554-562.
54. Y. Cheng, S. Lu, H. Zhang, C. V. Varanasi and J. Liu, *Nano Lett*, 2012, **12**, 4206-4211.
55. S. Gong, L. Jiang and Q. Cheng, *Journal of Materials Chemistry A*, 2016, **4**, 17073-17079.
56. Y. Wen, M. Wu, M. Zhang, C. Li and G. Shi, *Advanced Materials*, 2017, **29**, 1702831.
57. S. Wan, Y. Li, J. Mu, A. E. Aliev, S. Fang, N. A. Kotov, L. Jiang, Q. Cheng and R. H. Baughman, *Proceedings of the National Academy of Sciences*, 2018, **115**, 5359-5364.
58. S. Wan, Y. Chen, Y. Wang, G. Li, G. Wang, L. Liu, J. Zhang, Y. Liu, Z. Xu, A. P. Tomsia, L. Jiang and Q. Cheng, *Matter*, 2019, DOI: https://doi.org/10.1016/j.matt.2019.04.006.
59. S. Y. Kim, J. Hong, R. Kavian, S. W. Lee, M. N. Hyder, Y. Shao-Horn and P. T. Hammond, *Energ Environ Sci*, 2013, **6**, 888-897.
60. J. F. Che, P. Chen and M. B. Chan-Park, *J Mater Chem A*, 2013, **1**, 4057-4066.
61. L. L. Zhang and X. S. Zhao, *Chem Soc Rev*, 2009, **38**, 2520-2531.
62. A. Sumboja, C. Y. Foo, X. Wang and P. S. Lee, *Advanced Materials*, 2013, **25**, 2809-2815.
63. Y. N. Li, G. Y. Ren, Z. Q. Zhang, C. Teng, Y. Z. Wu, X. Y. Lu, Y. Zhu and L. Jiang, *J Mater Chem A*, 2016, **4**, 17324-17332.
64. P. G. Whitten, G. M. Spinks and G. G. Wallace, *Carbon*, 2005, **43**, 1891-1896.

65. J. N. Barisci, G. G. Wallace and R. H. Baughman, *J. Electroanal. Chem*, 2000, **488**, 92-98.
66. J. L. Rigueur, S. A. Hasan, S. V. Mahajan and J. H. Dickerson, *Carbon*, 2010, **48**, 4090-4099.
67. D. O'Brien, D. Baechle and E. J. J. o. C. M. Wetzel, *Journal of Composite Materials*, 2011, **45**, 2797-2809.
68. J. Snyder, E. Gienger and E. J. J. o. C. M. Wetzel, *Journal of Composite Materials*, 2015, **49**, 1835-1848.
69. H. Qian, H. Diao, N. Shirshova, E. S. Greenhalgh, J. G. H. Steinke, M. S. P. Shaffer and A. Bismarck, *Journal of Colloid and Interface Science*, 2013, **395**, 241-248.
70. C. Shi, T. Wang, X. Liao, B. Qie, P. Yang, M. Chen, X. Wang, A. Srinivasan, Q. Cheng, Q. Ye, A. C. Li, X. Chen and Y. Yang, *Energy Storage Materials*, 2019, **17**, 136-142.
71. G. Qian, B. Zhu, X. Liao, H. Zhai, A. Srinivasan, N. J. Fritz, Q. Cheng, M. Ning, B. Qie, Y. Li, S. Yuan, J. Zhu, X. Chen and Y. Yang, *Advanced Materials*, 2018, **30**, 1704947.
72. Q. Chen, X. Li, X. Zang, Y. Cao, Y. He, P. Li, K. Wang, J. Wei, D. Wu and H. Zhu, *RSC Advances*, 2014, **4**, 36253-36256.
73. C. Zhong, Y. Deng, W. Hu, J. Qiao, L. Zhang and J. Zhang, *Chemical Society Reviews*, 2015, **44**, 7484-7539.

This journal is © The Royal Society of Chemistry 20xx

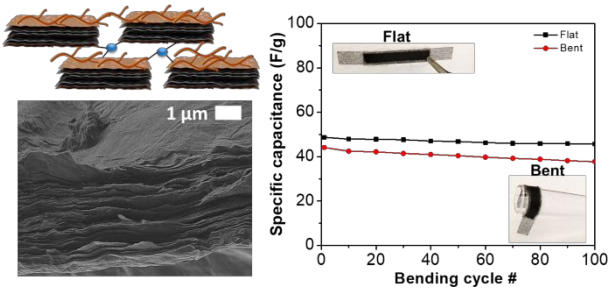

Noncovalent bonding of graphene/aramid nanofiber electrodes with tannic acid leads to enhanced mechanical properties while maintaining good energy storage